Journal of *Marine Science and Engineering*

MDPI

Article

Morphological Reconstruction Based on Optical Images for the Seabed Semi-Buried Polymetallic Nodules: A Fusion Model of Elliptic Approximation and Contour Interweaving Methods

Xiang Meng [1,2], Kehong Yang [2,*], Mingwei Wang [2,*], Qian Yu [1], Jihong Shang [2] and Ziyin Wu [2]

[1] Ministry of Education, Key Laboratory for Coast and Island Development, School of Geography and Ocean Science, Nanjing University, Nanjing 210093, China; xiangmeng@smail.nju.edu.cn (X.M.); qianyu@nju.edu.cn (Q.Y.)

[2] State Key Laboratory of Submarine Geoscience, Second Institute of Oceanography, Ministry of Natural Resources, Hangzhou 310012, China; jhshang@sio.org.cn (J.S.); zywu@sio.org.cn (Z.W.)

* Correspondence: yangkh@sio.org.cn (K.Y.); wangmw@sio.org.cn (M.W.)

Abstract

Polymetallic nodules enriched in Mn, Ni, Cu, Co, and other metals may be one of the first seabed mineral resources to be exploited. Although optical imagery is crucial for resource evaluation, semi-buried nodules are frequently overlooked. To address this, we propose a framework that integrates the elliptic approximation method (EAM) and the contour interweaving method (CIM) to reconstruct three types of semi-buried nodules segmented by U-Net: edge-buried, partition-buried, and almost-completely-buried. This strategy introduced a decision-making mechanism based on category fusion, which significantly enhanced the robustness and practicality of the reconstruction. Performance was assessed using four metrics: area ratio, absolute percentage change, intersection-over-union, and Chamfer distance. Among 1785 samples, the EAM recovered up to 41.8% of lost area, which substantially improved the minimum values of area ratio and intersection-over-union, and it performed well on almost-completely-buried nodules. The CIM achieved median area ratio and intersection-over-union values of 99.37% and 93.36%, respectively, and excelled in edge-buried and partition-buried types. Fusion experiments demonstrated the complementary strengths of both approaches: 23.96% of buried area was recovered in large-scale imagery recognized by U-Net. The proposed framework balances accuracy, adaptability, and computational efficiency, which enables real-time nodule identification on platforms with limited resources such as autonomous underwater vehicles. This could provide more direct support for resource evaluation and mining applications.

Keywords: U-Net; optical images; morphological reconstruction; semi-buried polymetallic nodules

Check for updates

Academic Editor: Jianhong Ye

Received: 27 November 2025
Revised: 19 December 2025
Accepted: 23 December 2025
Published: 26 January 2026

Copyright: © 2026 by the authors. Licensee MDPI, Basel, Switzerland. This article is an open access article distributed under the terms and conditions of the Creative Commons Attribution (CC BY) license.

1. Introduction

Polymetallic nodules (PMNs), also referred to as ferromanganese nodules, are widely distributed on the seabed at depths of 4000–6000 m in the global ocean and are rich in a variety of metallic elements such as Mn, Fe, Ni, Cu, Ti, and Co [1,2]. As an important deep-sea mineral resource, nodules can be used as a land-based alternative source of metal resources in the future [3–5].

PMNs are predominantly ellipsoidal, contain different morphologies, and are typically a few centimeters to a dozen centimeters in diameter [6]. Meyer et al. [7–9] classified

nodules into S (smooth) type, R (rough) type, and S-R (smooth-rough) type based on their morphology, size, and surface structure. In terms of shape, R-type nodules are predominantly globular, poplar, and renal; S-type nodules are mainly globular, multinucleated conidia, and irregular; and S-R-type nodules are mostly asymmetric ellipsoidal, resembling cauliflower. In addition, some nodules have irregular shapes such as triangles, arrows, and squares [10].

PMNs are among the seabed mineral resources most likely to achieve commercial exploitation first; therefore, their resource assessment studies are of significant interest. Advances in seabed acoustic remote sensing and near-bottom optical imaging technologies have enabled the identification and local assessment of nodule distribution based on image data [11–13]. Early research primarily relied upon traditional image processing methods, such as the non-learning morphological algorithm CoMoNoD [14]. With the development of deep learning, models such as MaskR-CNN and Pix2PixHD have significantly improved segmentation accuracy [15,16]. To reduce high annotation costs, semi-supervised methods have been introduced, such as diffusion models guided by limited labels [17]. A trained model utilizing the U-Net convolutional neural network to process seafloor images substantially improves the efficiency (processing 30,000 images within 10 h) and accuracy; however, there are recognition difficulties caused by sediment coverage [18]. Notably, most existing seafloor PMN identification studies focus on improving model accuracy for exposed nodules, and often neglect the critical challenge of semi-buried nodules [19]. This limits their capability to classify, reconstruct, and evaluate buried targets, which can introduce significant bias into resource assessments. Burial depth is linked to apparent number density, coverage, and size, which has a significant influence on nodule resource estimation [20]. In the Clarion–Clipperton zone, 20–50% of nodules may be partially or completely buried, with localized rates exceeding 60% [21]. In optical images, sediment typically obscures 10–40% of the nodule surface, and over 50% in extreme cases [22,23]. Collectively, these findings show that it is critical to accurately identify semi-buried nodules and highlight the need to develop robust methods to improve the accuracy of resource evaluation.

In response to this challenge, several studies attempted to address the underestimation of buried nodules. For instance, coverage underestimation was mitigated by morphological dilation, wherein an equivalent circle diameter fitting method estimated buried portions based on exposed nodule dimensions and collinearity theory [24]. While this approach partially compensates for coverage loss, the simplistic circular fitting often deviates significantly from the actual nodule morphology, which indicates a need for more geometrically adaptive reconstruction techniques.

To address the limitations of existing approaches in reconstructing semi-buried nodules, this study integrates U-Net segmentation with a feature-driven classification of nodule types and proposes two novel reconstruction methods: the elliptic approximation method (EAM) and contour interweaving method (CIM). By combining these two methods, the reconstructed nodules exhibit shapes and areas that more closely reflect the actual morphology. Comparative analyses demonstrate that the fused approach outperforms U-Net alone and achieves consistent results across binary and U-Net-segmented images, which confirms its robustness. These findings provide a more reliable basis for the analysis of nodule characterization based on optical images, and significantly enhance the accuracy of resource assessment.

2. Data

2.1. Data Source

The dataset used in this study was provided by the National Marine Data and Information Service, which was primarily obtained from the images captured by the underwater

camera vehicle of the DY69 cruise (Figure 1). After extracting a number of frames from the MP4 video, 618 images were obtained in PNG format. All images were preprocessed (illumination normalization, color cast removal, and perspective rectification) and normalized to dimensions of 512 × 512 px at 192 dpi resolution. On average, each image contained about 145 PMNs, which included semi-buried types, and yielded a total of approximately 90,000 nodules. Of these, 4583 (over 5%) were semi-buried nodules. Their grain sizes were predominantly concentrated between 3–6 cm, and their water depths ranged from 4840–5718 m.

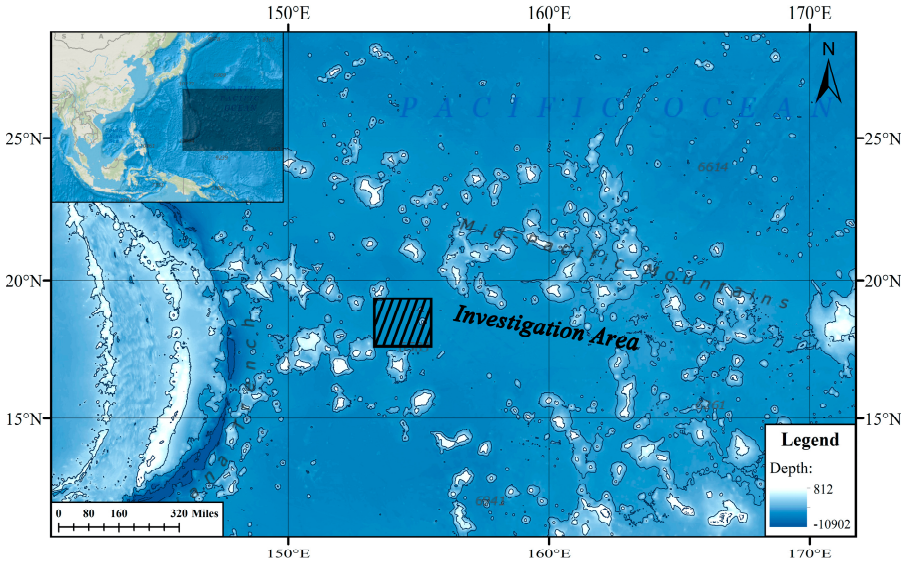


Figure 1. The main area for collecting images (the black shaded part).

2.2. Data Classification

According to the burial positions of PMNs in the image and the degree of burial, the types of semi-buried nodules were categorized into five types: edge-buried (EB), interior-buried (IB), partition-buried (PB), almost-completely-buried (ACB), and thin-sediment-covering (TSC) (Figure 2). Based on the results of U-Net training, IB and TSC can be effectively recognized [18]. Therefore, the semi-buried nodule types studied in this paper were EB, PB, and ACB.

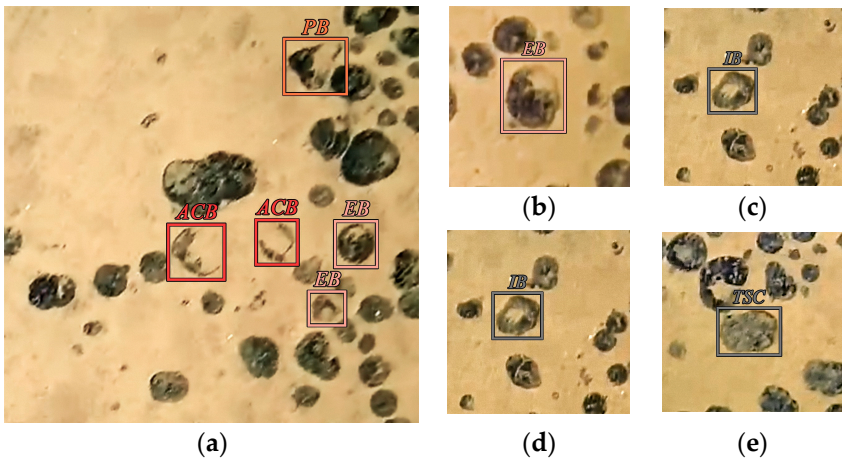


Figure 2. Polymetallic nodules (PMNs) in the seabed images. (**a**) Multiple semi-buried nodule types: (**b**) edge-buried (EB) type; (**c**) interior-buried (IB) type; (**d**) partition-buried (PB) type; (**e**) thin-sediment-covering (TSC) type.

EB refers to discontinuous edges of the nodules that are notched (Figure 2a,b), like the appearance of an apple with a bite taken out of it, and it retains ≥50% of the information overall (including the shape and area). PB refers to complete nodules being "split" into several parts in the image (Figure 2a,d), which can be caused by various factors, including occlusion by other objects, or splitting of the nodules by their own texture. PMNs can appear split in imagery (owing to occlusion, texture, or lighting), which may inflate apparent counts and reserves [25,26]. ACB means that most of one nodule is buried, with only a small portion of the nodule exposed (Figure 2a), and ≤30% of the information is generally retained, which is less abundant than the EB type, but more abundant than the PB type.

2.3. Data Selection and Preprocessing

The PMN dataset employed in this study was systematically collected from three representative seafloor topography units in the Pacific Ocean: abyssal plains/basins, seamounts, and abyssal slopes (Figure 3). This deliberate site selection strategy endows our dataset with robust geographic diversity, which provides a solid and representative platform for subsequent comparisons between U-Net and the reconstruction algorithm proposed herein. This ensures that our research conclusions are universal and reliable.

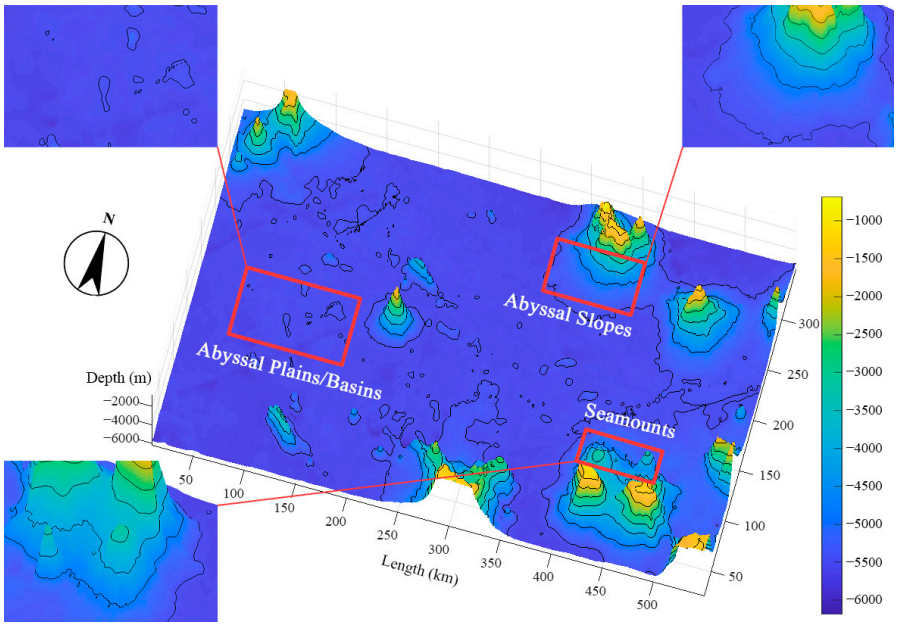


Figure 3. Selection criteria for the seabed environment.

After segmentation using U-Net (described in Section 3.1), the segmented semi-buried nodules were classified in Image Segmentation Annotation Tool, and each classified semi-buried nodule was extracted separately in Python 3.8.20 to obtain an extracted image with a size of 400 × 400 px and a resolution of 192 dpi in PNG format. Among the 618 images of PMNs, there were 4583 semi-buried nodules, with the EB type accounting for 3492 (76.2%) of these, the ACB type included 634 (~13.8%), while the PB type contained 457 (~10.0%).

A portion of semi-buried nodule samples were excluded from the reconstruction process owing to the absence of their true areas (defined as those determined through manual identification). The artificial identification of semi-buried nodules in a given area was jointly determined by the results annotated by four members within the research team (taking the range of annotation agreement). From 4583 semi-buried nodules, we selected 1785 samples for reconstruction experiments, which comprised 1466 EB nodules, 235 PB nodules, and 84 ACB nodules (Table 1). Considering that the positions of the semi-buried nodules in the image (boundaries and non-boundary regions) would affect

the reconstruction results, 159 semi-buried nodules located at the image boundaries were selected to separate experiments. That is, 1626 samples were located within the image, while 159 samples were at the edge of the image.

Table 1. Statistics of semi-buried nodule types used for reconstruction experiments.

Type	Number	Proportion	N_Max (Single Image)	N_Min (Single Image)
EB	1466	82.13%	11	1
PB	235	13.17%	4	0
ACB	84	4.70%	3	0

3. Methods

In morphological analysis of individual PMNs, key planar parameters include maximum diameter, minimum diameter, contour, and area [27]. Although partial shape and area information is lost in semi-buried states, we can still achieve reasonable morphological reconstruction based on the visible portions. To highlight the effectiveness of our method, we directly compared the reconstructed mask of semi-buried nodules with U-Net segmentation results. We propose the following hypothesis: a high-performance reconstruction method should more accurately restore nodule regions lost owing to burial.

To comprehensively evaluate the EAM and CIM against the U-Net segmentation results, we selected the following evaluation metrics: the ratio of reconstructed area to true area (AR), the absolute proportion of the difference between reconstructed and true areas relative to the true area (absolute percentage change, APC), the intersection-over-union ratio (IoU), and the Chamfer distance (CD). These metrics comprehensively measure the discrepancy between the reconstructed results and the true morphology in terms of area recovery, regional overlap rate, and contour similarity. The overall research workflow is illustrated in Figure 4.

3.1. Segmentation Method

U-Net architecture is a classical deep learning model that demonstrates strong learning capability and segmentation performance; therefore, it has been widely adopted in research and industrial applications [28]. We employed the standard U-Net architecture as the core segmentation network [29]. Its encoder–decoder structure with skip connections effectively captures local features and global contours of PMNs. Directly comparing our reconstructed results with their segmentation outputs offers the clearest means of quantifying the performance improvements introduced by the dedicated reconstruction step. For this reason, it was selected as the segmentation module and baseline model in this study.

The training process was conducted on a dataset containing 400 seafloor nodule images categorized into two classes (background and PMNs). The dataset was randomly split into training and validation sets in a 9:1 ratio. A two-phase training scheme was adopted to stabilize convergence. First, freeze training was performed using a small batch size of 4 for 100 epochs by freezing the backbone network. This was followed by unfreeze training where all network layers were unfrozen, which extended the total training to 200 epochs. To address the class imbalance between the foreground (nodules) and background (sediment-based), focal loss was chosen as the primary segmentation loss function. The Adam optimizer was used with an initial learning rate of 1×10^{-4}, and a cosine annealing schedule was applied to reduce the learning rate to a minimum of 1×10^{-6}. The number of data loading workers was set to 4 to improve data throughput efficiency.

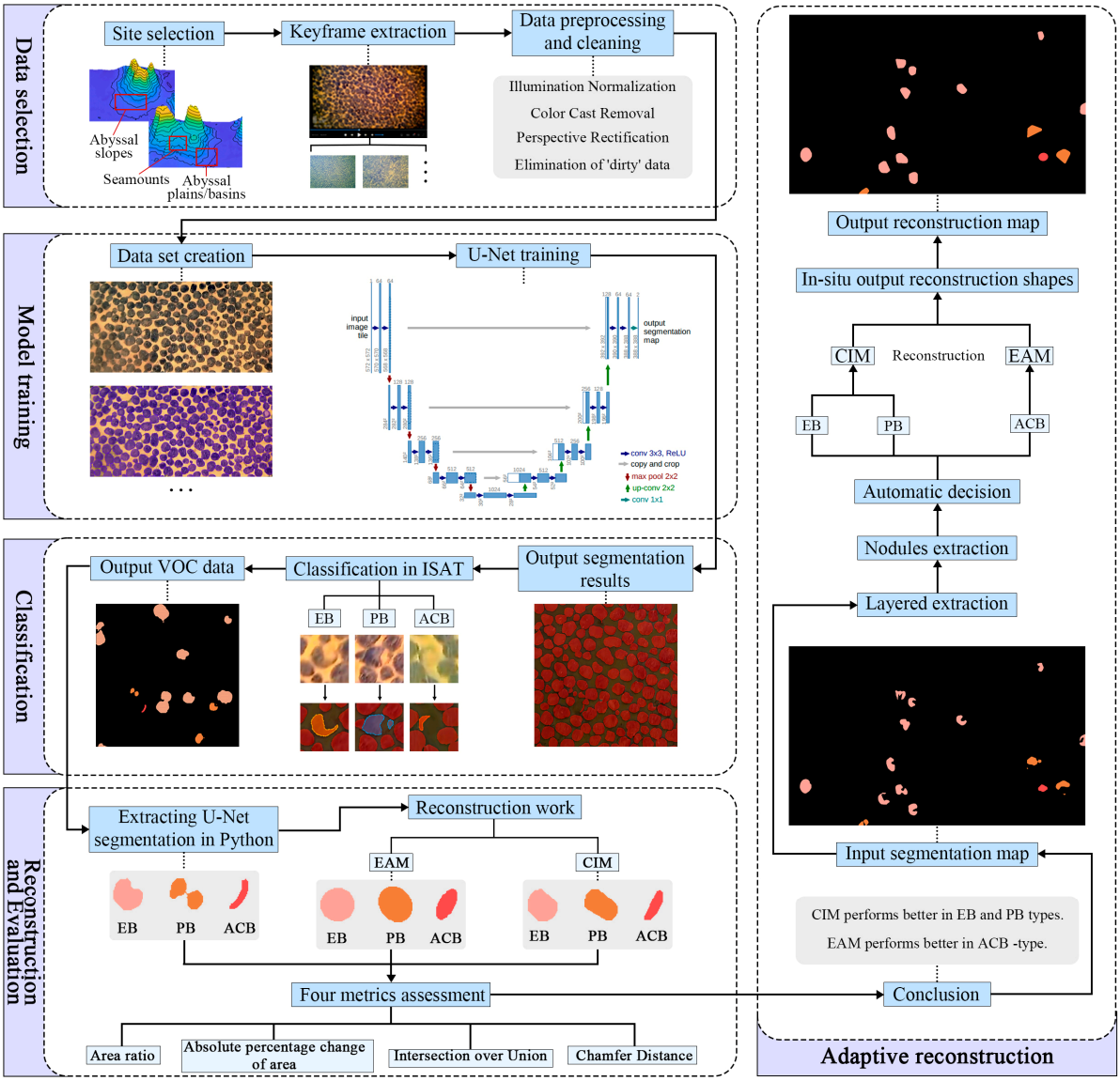
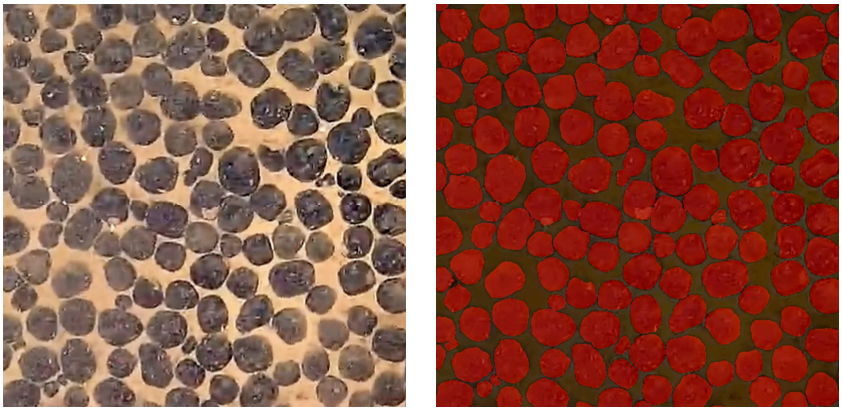


Figure 4. Overall research workflow.

Under this configuration, the trained U-Net model achieved strong preliminary segmentation performance on our dataset. Evaluation on an independent test set showed that the mean intersection-over-union steadily improved from an initial 90.2% to over 94.7%, while the loss value decreased rapidly and converged stably. This indicates that the model exhibits excellent and stable segmentation performance on unseen data, and provides a high-precision input basis for subsequent burial-type classification and multi-model fusion reconstruction (Figure 5). Furthermore, all images segmented by U-Net underwent an opening operation (erosion followed by dilation) to eliminate noise and non-nodule regions.



(**a**) (**b**)

Figure 5. PMN (including semi-buried types) segmentation after training images using U-Net: (**a**) the image before segmentation; (**b**) after segmentation.

3.2. Reconstruction Methods

3.2.1. Elliptic Approximation Method

Based on the general characteristics of PMNs, we assumed that the nodule morphology was elliptical in the ideal state. From the area of an ellipse ($S = \pi ab$), two important parameters that affect the size and shape of its area are the long and short axes. Taking the set of white pixels in a binary square image as $S = \{(x_i, y_i)|i = 1, 2, \ldots, N\}$, ellipse reconstruction was defined as follows:

1. Identifying the pair of white pixels $A(x_a, y_a)$ and $B(x_b, y_b)$ in the extracted image that are the farthest apart, the Euclidean distance between them, denoted as l, was defined as one of the axes of the ellipse:

$$l = \max_{A,B \in S} ||A - B||_2 = \sqrt{(x_b - x_a)^2 + (y_b - y_a)^2} \quad (1)$$

2. The midpoint O of line segment l was set as the center of the ellipse, and the white pixel $C(x_c, y_c) \epsilon S$ was determined, which maximized the perpendicular distance, d, to line segment AB, where AB was the segment previously defined. This distance d was defined as the half-length of the other axis:

$$d = \frac{\left|\vec{AB} \times \vec{AC}\right|}{l} = \frac{|(x_b - x_a)(y_c - y_a) - (y_b - y_a)(x_c - x_a)|}{\sqrt{(x_b - x_a)^2 + (y_b - y_a)^2}} \quad (2)$$

3. If $l/2 < d$, the long axis was set to $a = d$ and the short axis was $b = l/2$; otherwise, the long axis was assigned $a = l/2$ and the short axis was $b = d$.

Based on the steps described above, the initial ellipse was obtained after the following aspects were determined: its center, the position and length of one axis, and the length of the other axis. This ellipse reconstruction approach was employed to reconstruct the visible portions of semi-buried nodules. The complete reconstruction process is illustrated in Figure 6. When $a = b$, the ellipse represents a circle.

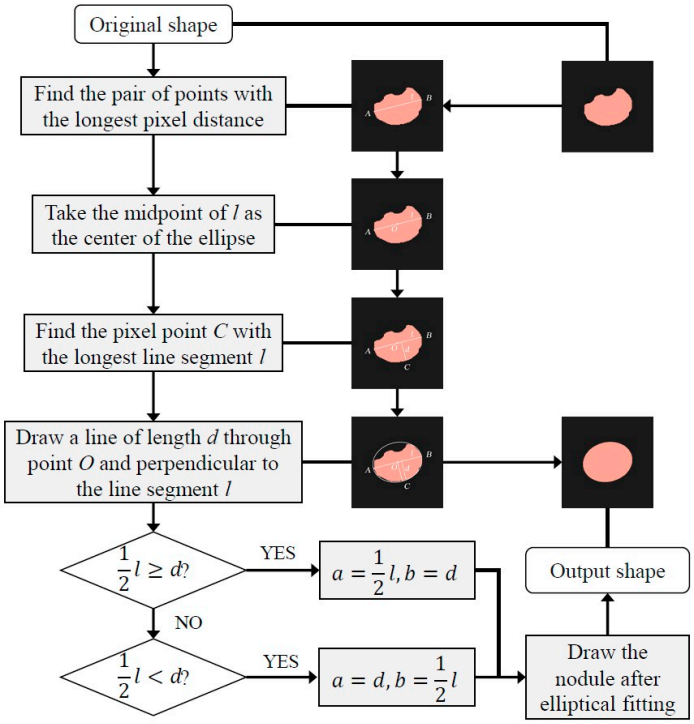


Figure 6. Reconstruction process of the elliptic approximation method (EAM).

While EAM is suitable for near-circular or elliptical nodules, the shapes of nodules often demand more sophisticated reconstruction methods to accurately represent their actual morphologies.

3.2.2. Contour Interweaving Method

The contour represents a critical morphological feature of semi-buried nodules. The mathematical foundation for contour extraction involves precise boundary point identification and tracking, where pixels are classified as contour elements to form a continuous boundary chain based on rigorous geometric criteria [30]. To ensure accurate morphological representation, the final extracted contour must exclude internal voids or nested structures and only retain the outermost contour.

For example, a binary image was supposed as matrix $I(x,y) = \{0,1\}$, where 1 (or 255) and 0 denoted a white foreground and black background, respectively, with the set of boundary points C defined as follows:

$$C = \{(x,y)|I(x,y) = 1 \wedge \exists(i,j) \in N(x,y), I(i,j) = 0 \quad (3)$$

where $N(x,y)$ was the 8-neighborhood of pixel (x,y). For a pixel to belong to the contour, at least one neighboring pixel must belong to the background.

All boundary points were extracted by erosion with a difference set operation, which shrinks the foreground region, and the difference set between the original image and the eroded image was the boundary [31,32]. The formula for the erosion operation was expressed below:

$$Erode(I,B) = I \ominus B = \left\{z \in \mathbb{Z}^2 | B_z \subseteq A\right\} \quad (4)$$

where B was a 3×3 all 1 structural element, and $B_z = \{b + z | b \in B\}$ was the set of structural elements B after translation. The boundary extraction formula was expressed as follows:

$$Boundary(I) = I - Erode(I,B) \quad (5)$$

Using the Moore–Neighbor boundary tracking algorithm, a closed contour was formed by connecting the boundary points sequentially [33]. The principle is to find the first unvisited boundary point $p_0 = (x_0, y_0) \in E$, define the search direction $d \in \{0, 1, \ldots, 7\}$ (corresponding to 8-neighborhood direction), search and find the next boundary point $p_{k+1} \in E \bigcap N_8(p_k)$ in a clockwise direction from the current point p_k, update $p_k = p_{k+1}$ and mark it as visited, and adjust the search direction (see Equation (6)) to continue searching when it was not found. When the $p_{k+1} = p_0$ path was closed, a closed sequence of contour points $C = \{p_0, p_1, \ldots, p_n\}$ was obtained:

$$d \equiv d + 1 \ (mod 8) \tag{6}$$

Since only the outermost contours need to be preserved, the hierarchical relationship between contours was utilized after searching all boundary points. Suppose that the set of all contours was $C_0, C_1, \ldots, C_n$, if another contour C_j existed in the region contained by contour C_i, then C_j was a subcontour of C_i, so that the outermost contour satisfied the following equation:

$$\forall C_i \neq C_j, \ Area(C_i) \not\subset Area(C_j) \tag{7}$$

In other words, the extracted outermost contour exists independently and is not enclosed by any other boundary segments. Through this procedure, the target contour is isolated from the binary image, effectively eliminating interference from internal holes and ancillary contours. The final output therefore represents the complete, unobstructed boundary of a semi-buried nodule.

Although the contour provides essential geometric information about a semi-buried nodule, an effective shape representation requires appropriate region filling after contour extraction. Given that PMNs predominantly exhibit convex geometric characteristics in the two-dimensional plane [34,35], based on this morphological prior, we propose the CIM as a novel shape completion approach specifically designed for semi-buried nodules. The core principle of CIM is to systematically connect each pixel on the contour with all other contour pixels, thereby efficiently constructing and filling the convex hull of the point set in a raster image. Mathematically, this operation extrapolates the sediment-covered portions of the nodule under the convexity assumption.

In practice, the contour is extracted as a set of n pixels. To construct its rasterized convex hull, all possible point pairs must be connected, yielding a total of $n(n-1)/2$ line segments. In the raster domain, each line segment between two points is approximated by identifying the discrete pixel path that best matches a continuous straight line. We adopt the classical Bresenham line-drawing algorithm (1965) to efficiently and accurately fill the pixels within the nodule region [36]. After all contour pixels have been iteratively connected, the pixel-wise union of these line segments forms the reconstructed two-dimensional shape, which serves as an estimate of the complete semi-buried nodule. Figure 7 illustrates the full workflow of CIM. Compared with conventional interior filling methods (e.g., flood fill), CIM produces reconstructions that more faithfully conform to the true convex geometry of PMNs, as it not only fills the interior but, more importantly, infers and reconstructs the missing external boundary based on the visible contour.

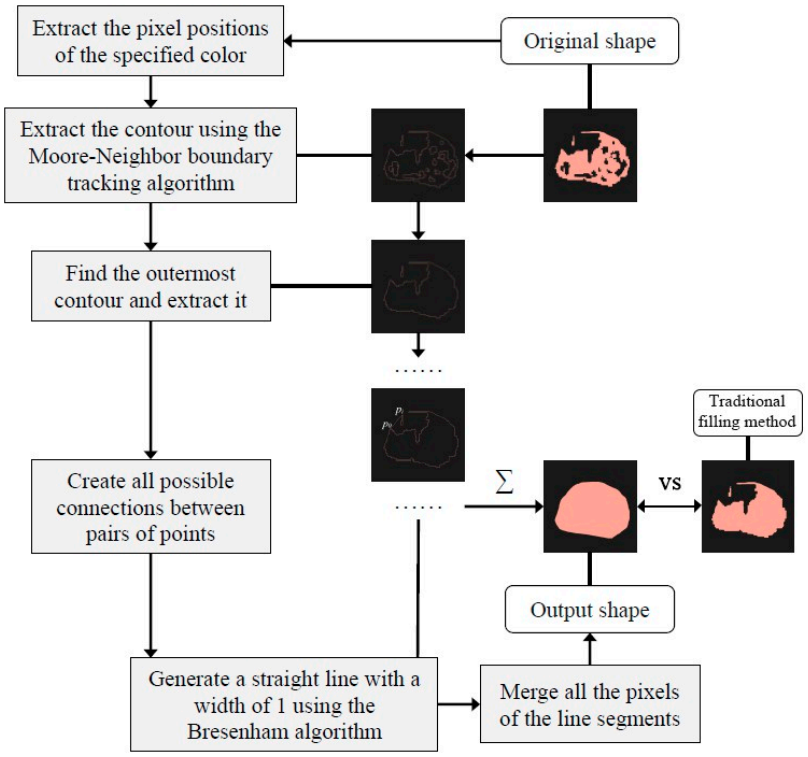


Figure 7. Reconstruction process of the contour interleaving method (CIM).

3.3. Evaluation Metric

3.3.1. Relative Area

In the resource evaluation of PMNs, the estimation of nodule area directly affects the quantity of resources. Since this study focused on comparing the reconstruction results with the true areas, two relative area-based metrics were used to reflect differences in the scale of the target area (the number of pixels of the specified color): AR and APC of the area. The target RGB value was denoted as (R_t, G_t, B_t). Considering that the actual pixel color may not exactly match the target color owing to image compression, anti-aliasing, or lighting variations, and a tolerance threshold T (a non-negative real number) were defined to allow the color to be considered as a match within a certain range of differences. For each pixel (i, j) in the image with RGB values of (R_{ij}, G_{ij}, B_{ij}), the color difference ΔE_{ij} from the target color was calculated as follows:

$$\Delta E_{ij} = \sqrt{(R_{ij} - R_t)^2 + (G_{ij} - G_t)^2 + (B_{ij} - B_t)^2} \tag{8}$$

where ΔE_{ij} was the Euclidean distance in RGB space, and a pixel was considered to match the target color if $\Delta E_{ij} \leq T$ [33].

If the width of the image was W pixels, the height was H pixels, and the total number of pixels was $W \times H$. Iterating over each pixel to calculate ΔE_{ij} and count the total number of matched pixels was expressed below:

$$N = \sum_{i=1}^{W} \sum_{j=1}^{H} 1\left(\Delta E_{ij} \leq T\right) \tag{9}$$

where $1(\cdot)$ was the indicator function, which had a value of 1 if the condition was true, otherwise it was assigned as 0. N was the relative area A_r.

Equation (10) showed the AR to the real shape, and it directly reflected the differences. The closer the ratio was to 1, the closer the match. If the ratio was greater than 1, the

reconstructed area exceeded the actual area; if the ratio was less than 1, the size of the reconstructed area was lower than the actual area.

$$AR = \frac{A_r(I)}{A_r(J)} \tag{10}$$

where $A_r(I)$ was the reconstructed area (or segmentation area), and $A_r(J)$ was the real area.

The absolute value of the ratio between the area difference of the reconstructed shape and the real shape to the real shape (see Equation (11)), referred to as the APC, was used to quantify the underestimation or overestimation of the reconstructed result. A ratio of 0 indicates an exact match in area, while larger values signify a greater discrepancy between the reconstructed results and the true areas.

$$APC = \frac{|A_r(I) - A_r(J)|}{A_r(J)} \tag{11}$$

3.3.2. Intersection-over-Union

The IoU was used to measure the degree of overlap between two regions and calculated as the ratio of the area (or number of pixels) of the intersection between the predicted region and the real region to the area of their concatenation, which quantified how well the predicted result matched or resembled the real situation [37] according to the following equation:

$$IoU(A, B) = \frac{A \cap B}{A \cup B} = \frac{\sum(A \odot B)}{\sum(A + B) - \sum(A \odot B)} \tag{12}$$

where A was the reconstructed area (or segmentation area), B was the real area, $(A \odot B)$ was a pixel-by-pixel logical and operation, and $A \cup B$ was a logical or operation.

The IoU can reflect the proportion of overlapping regions to the total coverage of the two regions, and its value domain was [0, 1]. An IoU of 100% indicates that the two regions completely overlap, while 0% shows that the two regions do not overlap. The closer the value is to 1, the higher the overlap with the ground truth and the more accurate the prediction.

3.3.3. Chamfer Distance

The CD is a measure of shape similarity between two point-sets (such as contour points of a binary image) that captures the geometric differences in shape by calculating the bidirectional average nearest-neighbor distance between two point-sets [38]. Since only the morphological differences between the reconstructed nodules and the real nodules were considered in this study, the full images were normalized to eliminate the effect of different sizes on the values [39]. For two point-sets P and Q, the CD was given by the following equation:

$$CD(P, Q) = \frac{1}{2}\left(\frac{1}{|P|}\sum_{p \in P} \min_{q \in Q} ||p - q|| + \frac{1}{|Q|}\sum_{q \in Q} \min_{p \in P} ||q - p||\right) \tag{13}$$

where $|P|$ denoted the base (number of points) of the point-set P, $|Q|$ was the base of the point-set Q, $||p - q||$ was the Euclidean distance between points p and q, $\min_{q \in Q} ||p - q||$ was the one-way mean nearest distance from the point-set P to Q, and $\min_{p \in P} ||q - p||$ was from the point-set Q to P.

The smaller the value of this distance, the more similar the shapes were between the two graphs, while the larger the value, the more significant the difference [38]. When two

shapes were identical, the value was 0. The magnitude of CD value is related to the size and resolution of the image [40]. For an image with a size 400 × 400 px and a resolution 192 dpi, its diagonal length was 565.68 px (the upper limit of the distance value) using the empirical grading method. The general evaluation criteria of the CD are shown in Table 2.

Table 2. Reference evaluation criteria for Chamfer distance (CD).

Value Range	Similarity Evaluation	Explanation
[0, 0.05)	Excellent	Almost overlapping
[0.05, 0.15)	Very good	Highly matched
[0.15, 0.3)	Good	Well-corresponding
[0.3, 0.6)	Pass	Out of alignment
[0.6, 1.2)	Poor	Obvious offset
[1.2, 2.5)	Very poor	Significantly mismatched
≥2.5	Extremely poor	Completely mismatched

4. Results

The 1626 semi-buried nodules within the image were reconstructed in Python using the EAM and CIM for three burial types: EB, PB, and ACB. For each nodule, four images were generated based on the extracted shape: ellipse contour, original contour, ellipse filling, and contour interweaving. In case of ACB-type nodules, the EAM provided higher median values of AR (58.96%) and IoU (54.53%) than the CIM (45.39% and 43.45%, respectively). The CIM provided reconstructed shapes that appeared to resemble the correct morphology for EB and PB types (as shown in Figure 8). After reconstruction, calculations were performed on four metrics (AR, APC, IoU, and CD) for the U-Net segmentation versus true shapes, the EAM images versus true shapes, and the CIM images versus true shapes. Following the calculations, statistics were compiled for the values of maximum, minimum, mean, median, and standard deviation (Table 3).

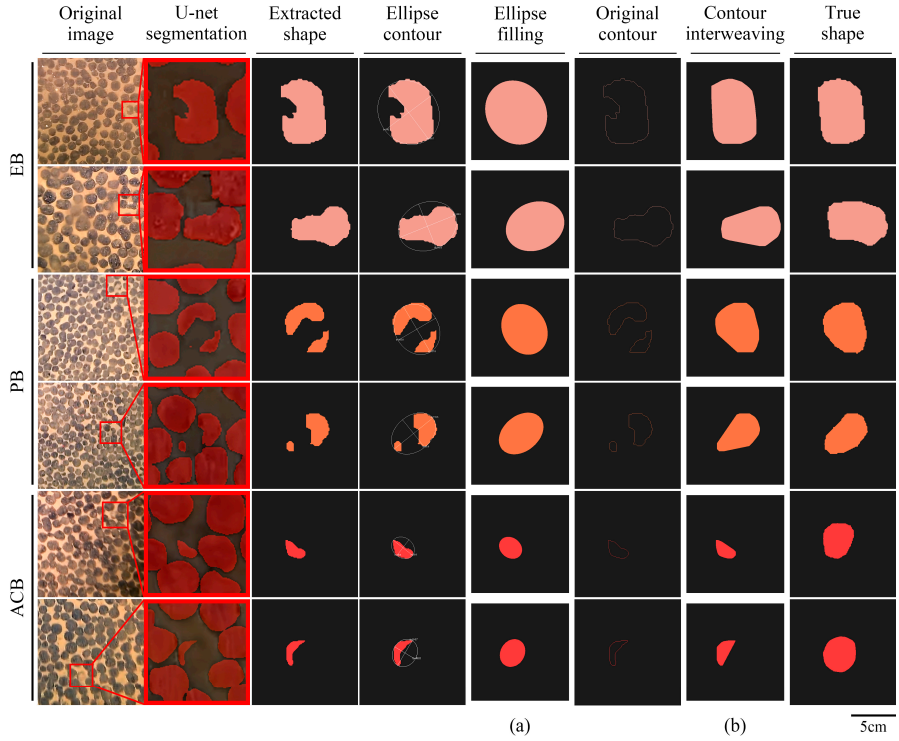


Figure 8. Comparing the pictures of different types of semi-buried nodules: (**a**) is the image generated by the elliptic approximation method (EAM); (**b**) is the image generated by the contour interweaving method (CIM).

Table 3. U-Net versus two reconstruction methods on each metric (non-boundary regions).

Metric	Semi-Buried Type	Method	Maximum	Minimum	Mean	Median	Standard Deviation
Area ratio (AR)	EB	U-Net	94.99%	41.56%	84.99%	88.11%	0.1077
		EAM	184.63%	58.20% *	116.27%	115.91%	0.1546
		CIM	113.18%	46.31%	95.29%	98.42%	0.0939
	PB	U-Net	91.59%	32.66%	64.32%	64.86%	0.1599
		EAM	173.99%	74.46%	121.32%	118.88%	0.1942
		CIM	108.86%	53.83%	95.56%	99.37%	0.1125
	ACB	U-Net	67.62%	14.78%	38.72%	38.02%	0.1196
		EAM	115.06%	25.98%	63.56%	58.96%	0.2139
		CIM	74.64%	21.03%	47.15%	45.39%	0.1473
Absolute percentage change (APC)	EB	U-Net	58.44%	3.01%	15.01%	11.89%	0.1077
		EAM	84.63%	0.04%	18.53%	16.74%	0.1267
		CIM	53.68%	0.02%	6.67%	3.32%	0.0812
	PB	U-Net	67.34%	8.41%	35.68%	35.14%	0.1599
		EAM	73.99%	1.48%	24.24%	20.94%	0.1552
		CIM	46.17%	0.03%	7.56%	4.19%	0.0939
	ACB	U-Net	85.22%	32.38%	61.28%	61.98%	0.1196
		EAM	74.02%	5.75%	37.51%	41.04%	0.1937
		CIM	78.97%	25.36%	52.85%	54.6%	0.1473
Intersection over Union (IoU)	EB	U-Net	92.99%	40.56%	84.68%	85.89%	0.1089
		EAM	95.73%	48.47%	80.25%	81.3%	0.0794
		CIM	98.32%	44.81%	89.94%	93.22%	0.0844
	PB	U-Net	91.59%	32.54%	64.15%	64.86%	0.1624
		EAM	88.25%	56.67%	76.62%	76.45%	0.0746
		CIM	97.68%	50.34%	89.06%	93.36%	0.0963
	ACB	U-Net	66.82%	14.17%	38.36%	37.58%	0.1195
		EAM	92.55%	24.76%	55.26%	54.53%	0.178
		CIM	71.38%	18.41%	45.06%	43.45%	0.1426
Chamfer distance (CD)	EB	U-Net	5.8005	0.0321	0.4918	0.2628	0.6092
		EAM	3.3813	0.0277	0.4806	0.3306	0.4747
		CIM	5.3454	0.009	0.2332	0.0718	0.4361
	PB	U-Net	3.4578	0.1086	1.0937	0.8751	0.7699
		EAM	1.6005	0.1092	0.5308	0.4491	0.3586
		CIM	2.4563	0.0124	0.1788	0.0593	0.4021
	ACB	U-Net	8.4514	0.6022	3.6148	2.7093	2.4063
		EAM	5.9934	0.0872	1.783	1.3073	1.4673
		CIM	7.2134	0.4754	2.9083	2.5492	1.9892

* The red values represent the optimal values of the two reconstruction methods in the same statistical function for each category of metrics. The blue values are presented in the Discussion.

For 159 semi-buried nodules located at image edges, an additional cropping step is required after EAM reconstruction before outputting the cropped shape, as illustrated in Figure 9. Statistical analysis does not distinguish between different types of semi-buried nodules owing to the limited overall sample size of such nodules and the absence of ACB types. The semi-buried nodules located at image edges were reconstructed using the EAM and CIM, and the results are presented in Table S1.

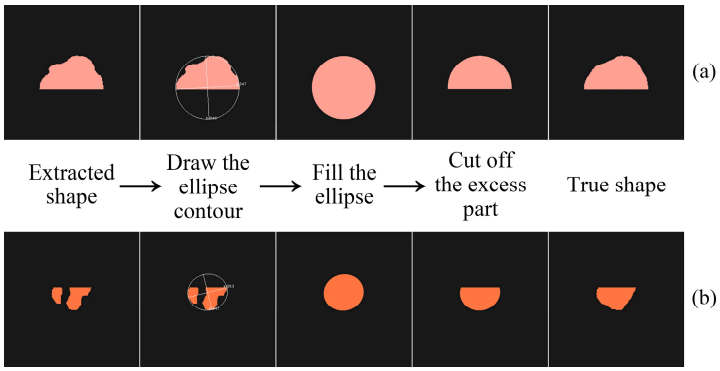


Figure 9. Reconstruction process of semi-buried nodules located at the image boundaries using the EAM: (**a**) EB type; (**b**) PB type.

4.1. Results of the EAM

Within the image and compared to U-Net segmentation nodules, the EAM significantly improved the minimum AR values for various semi-buried nodule types: the EB type, PB type, and ACB type increased by 16.64%, 41.8%, and 11.2%, respectively. However, this method overestimated the reconstructed area, which exceeded the actual area by 84.63% in extreme cases. For the ACB type, this method reduced the minimum value of APC from 32.38% to 5.75%, which effectively minimized the area difference. Regarding the IoU, the EAM generally improved minimum values and increased the maximum IoU for the ACB type by 25.73%. The average and median IoU values for the PB type increased by approximately 12%, and about 17% for the ACB type. Regarding CD, the EAM reduced the maximum value for most types and lowered the minimum value for the ACB type from 0.6022 to 0.0872, which improved the performance from "poor" to "excellent" (Table 3).

For samples near image edges, the EAM improved the minimum AR by 32.61%, although the exceeded area reached 122.39%. Concurrently, the minimum APC decreased from 3.34% to 0.97%, and the average and median values declined. The average and median IoU values increased by approximately 2%. The minimum CD decreased from 0.1351 to 0.0325, which indicated that some reconstructed results more closely approximated the true shape. However, the maximum value increased from 2.9101 to 5.0425, which revealed more significant shape alterations in some samples (Table S1).

4.2. Results of the CIM

The CIM demonstrated superior overall performance despite showing less pronounced improvements in the AR and IoU minimums. Regarding the AR metric, both the mean and median (98.42%) values for the EB type increased by approximately 10%. For the PB type, the mean value rose by 31.24%, while the median (99.37%) increased by 34.51%. Regarding APC, the CIM substantially reduced the mean and median values for the EB and PB types. For instance, the mean decreased from 35.68% to 7.56%, which indicated that it effectively narrowed the gap between the reconstructed area and true values. For the IoU, the EB type achieved a maximum of 98.32% and the median increased by 7.33%; for the PB type, the maximum reached 97.68% and the median increased by 28.5%, which indicated that the IoU ratio exceeded 90% for most samples. Regarding CD, the minimum for the EB type dropped to 0.009 (excellent), with a median of 0.0718 (good); the mean for the PB type decreased from 1.0937 to 0.1788, while the median decreased from 0.8751 to 0.0593, which indicated that CIM more closely approximated true shapes in morphological reconstruction (Table 3).

For image edge samples, the CIM increased the AR by 13.9% to 95.52%, and the median rose by 12.38% to 97.81%. The maximum and minimum APC decreased from

52.92% to 33.94% and from 3.34% to 0.05%, respectively, and the mean and median values significantly declined. The minimum IoU improved by 17.48%, while the mean and median values increased by approximately 10%, and reached a maximum of 98.29%. The minimum CD decreased to 0.0089 (excellent), and the average dropped from 0.6699 to 0.2112, which resulted in the median falling from 0.3915 to 0.0476, and indicated that this method significantly improved shape-matching performance (Table S1).

4.3. Comparison of the Two Reconstruction Methods

Among the 1626 samples within the images, the performance of CIM and EAM across all metrics is shown in Figure 10. Regarding the AR, the CIM results primarily distributed between 85% and 105%, while the EAM results clustered between 105% and 190%, with the maximum value approaching twice the true area. For APC, the CIM clustered between 0% and 5%, while the EAM was between 10% and 40%. Regarding IoU, the CIM achieved values above 90% in 1043 samples, whereas the EAM mostly ranged between 60% and 90%. Regarding CD, over 60% of samples from the CIM fell within the "excellent" to "good" range, whereas only about 16.5% from the EAM achieved "excellent" or higher ranges, and over a quarter performed poorly.

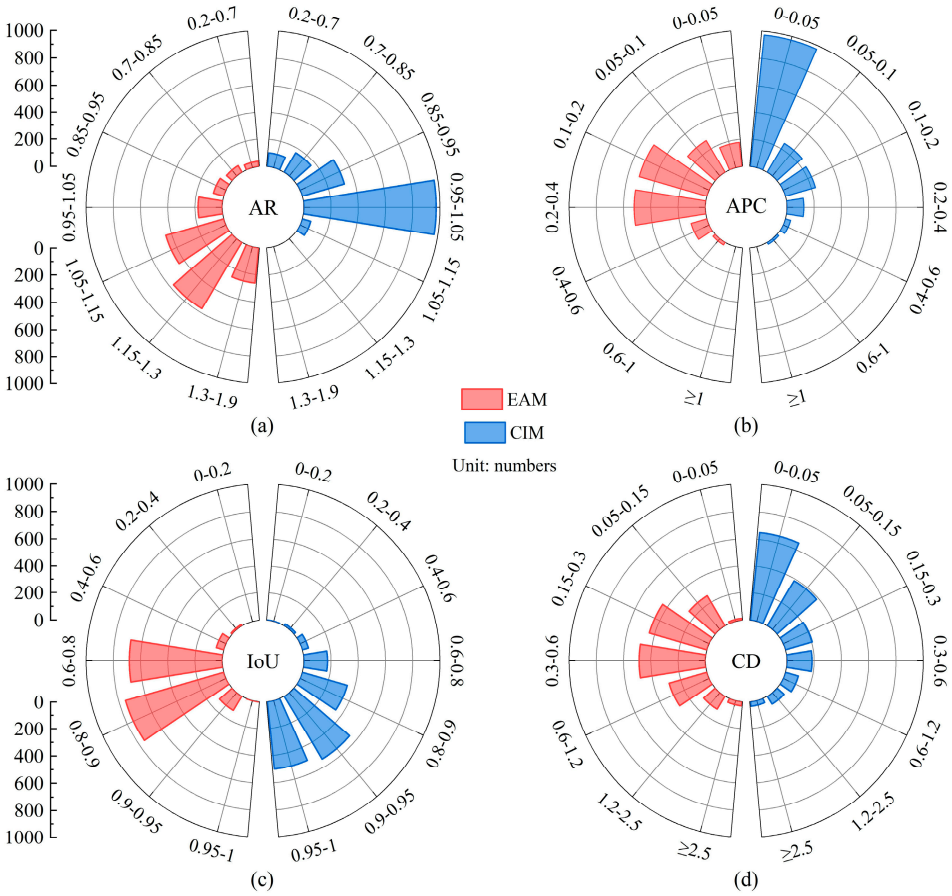


Figure 10. Comparison of the distribution of the two reconstruction methods on the four metrics (non-boundary regions). The number count of the two methods (EAM and CIM): (**a**) AR; (**b**) absolute percentage change (APC); (**c**) intersection-over-union (IoU); and (**d**) Chamfer distance (CD).

For 159 edge samples, the CIM narrowed the ranged of AR to between 85% and 105%, and APC decreased as the interval increased; the EAM showed more dispersed distributions for AR and APC. Regarding IoU, the CIM exceeded 80% in approximately 90% of samples, while the EAM primarily ranged between 80% and 90%. For CD, nearly half of the CIM samples were "excellent," whereas only about a quarter of the EAM samples

were "excellent" or higher, which further demonstrated the CIM's superior performance in shape representation (Figure 11).

To quantitatively evaluate the performance differences among the proposed reconstruction methods, a systematic statistical analysis was conducted on the core metrics for all intra-image samples (N = 1626). As the data did not satisfy the assumption of normality, the non-parametric Wilcoxon signed-rank test was employed, with the significance level set to $\alpha = 0.05$.

For the statistical analysis of polymetallic nodule area (in pixels), the results indicate that EAM reconstructs significantly larger nodule areas than U-Net in nearly all samples, with a consistent improvement on the order of approximately 1000 pixels. This difference is not only statistically significant but also of substantial practical significance. CIM also significantly outperforms U-Net in terms of reconstructed area; however, the magnitude of improvement is notably smaller than that of EAM, representing a moderate yet highly stable enhancement. For IoU metric, the statistical results demonstrate that EAM significantly outperforms U-Net in overall region overlap accuracy. Compared with the area metric, the magnitude of improvement is more moderate, suggesting that EAM primarily enhances region recovery rather than fine-grained boundary precision. CIM shows a statistically significant and very large effect size improvement over U-Net in IoU, indicating a more concentrated and consistent gain in region overlap accuracy. For Chamfer distance (CD), the results show that EAM only marginally improves the Chamfer distance with a negligible effect size, implying limited gains in contour alignment. In contrast, CIM significantly reduces the Chamfer distance, indicating a clear advantage in contour geometry consistency and boundary refinement.

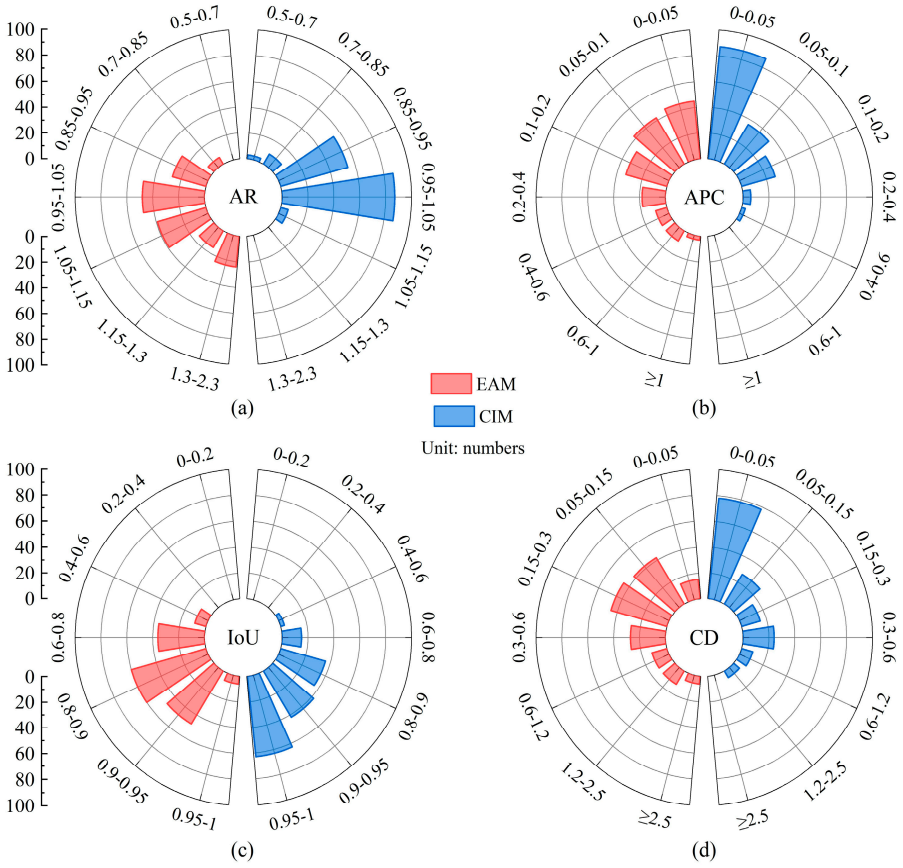


Figure 11. Comparison of the distribution of the two reconstruction methods (EAM and CIM) on the four metrics (boundaries region). The number count of the two methods: (**a**) AR; (**b**) APC; (**c**) IoU ratio; and (**d**) CD.

Overall, the statistical analysis confirms, at the 95% confidence level, that significant differences exist among the compared methods across most key evaluation metrics. The detailed statistical results are summarized in Table 4.

Table 4. Significant statistical analysis of the reconstruction results.

Metric	Comparison Method	Z	*p*-Value	r	95% CI	Significance
Area	U-Net vs. EAM	−34.791	<0.001	0.863	[−1059.5, −988.0]	Yes
	U-Net vs. CIM	−34.755	<0.001	0.862	[−313.0, −292.0]	Yes
IoU	U-Net vs. EAM	−16.239	<0.001	0.403	[0.0501, 0.0609]	Yes
	U-Net vs. CIM	−33.154	<0.001	0.822	[−0.0321, −0.0288]	Yes
CD	U-Net vs. EAM	−2.049	0.040	0.051	[−0.0594, −0.0168]	Yes
	U-Net vs. CIM	−34.720	<0.001	0.861	[0.1268, 0.1406]	Yes

5. Discussion

Given that the true geometric shape of the buried portions cannot be directly observed, this study adopts a multi-expert–based "consensus ground truth" as the evaluation reference in order to establish a rigorous assessment framework under current technical constraints. By jointly employing complementary quantitative metrics at the macroscopic (area), global (IoU), and local (CD) levels, we perform relative comparisons of different algorithms in terms of their agreement with expert consensus. Through the combination of a consensus mechanism and multiple evaluation metrics, these methods maximize the scientific validity and reliability of the conclusions. The dataset used in this study encompasses seabed imagery from diverse geomorphological settings, as well as nodules of varying sizes and types. Nevertheless, as all data were acquired during a single cruise, certain limitations may remain. In future work, we will seek additional datasets to further extend and strengthen the proposed methodology.

The results clearly revealed that most nodule areas obtained by the EAM exceeded the true area, with extreme cases doubling it, while the IoU and CD generally fell short of the CIM's performance (Figures 10 and 11). However, the EAM markedly improved the minimum values of AR and IoU. For the ACB type, the EAM outperformed CIM across all metrics (Tables 3 and S1), which indicated its distinct advantage when larger portions of nodules were buried (Figure 8a). The EAM performed well when the true shape was closer to a circle or ellipse. Additionally, there was an unusually high AR index value of 115.06% during EAM reconstruction of an ACB nodule. Upon careful examination, this discrepancy arose because the calculated major and minor axes of the ellipse for the exposed portion of the nodule were larger than the actual dimensions (Figure 12a). However, this method has limitations for PMNs exhibiting highly irregular shapes. For example, the EAM overestimated the actual area of intergrown nodules—which deviated most significantly from the ideal ellipse—by approximately 20% to 80%, with considerable morphological variation (Figure 12b). This limitation similarly applies to other distinctly non-elliptical shapes, such as cauliflower-like, highly elongated, or triangular morphologies. In subsequent work, we aim to optimize the EAM to enhance its reconstruction capability for intergrown nodules.

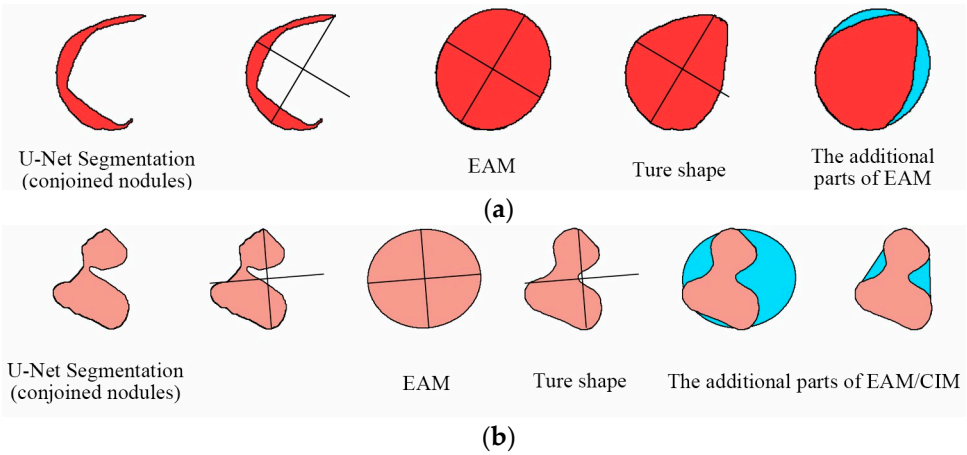


Figure 12. Some of the reconstruction results exceed the actual values: (**a**) examples of ACB type showing over-reconstruction after using EAM; (**b**) example of intergrown nodules (EB type) showing over-reconstruction after using EAM and CIM. Cyan indicates the over-reconstructed portion.

In contrast, the CIM enhanced the robustness of area estimates, with reconstructed results generally closer to reality and less prone to overfitting (Figure 8b). For PB and EB types, CIM proved highly effective (Tables 3 and S1), and recovered morphological features and outer contours more faithfully than EAM. However, CIM occasionally yielded excess areas, and the maximum AR values reached 113.18% for the EB type and 108.86% for the PB type (Table 3) and 106.39% in Table S1. This overestimation arises from intergrown or reniform nodules, where CIM fills regions not belonging to nodules (Figure 12b). Obviously, both approaches are likely to over-reconstruct for such intergrown nodules. This is a sign that a pre-classification stage could potentially look out for such complex geometries before EAM and CIM are used, perhaps by a measure of shape complexity. Reconstruction utilizing the skeleton extracted from exposed nodule parts may serve as a third reconstruction technique to be incorporated into the framework for handling highly irregular or intergrown nodules. Meanwhile, since the reconstructed edge of the CIM is not completely curved, it differs somewhat from the actual edge of the nodules, which is rounder. This is an area that can be improved in the future.

5.1. Reconstruction of Binary Images

To verify the versatility and effectiveness of the proposed methods, this study repeated the reconstruction process based on the original experiments with 71 binarized images of semi-buried nodules (with the threshold set to 120). A comparison of the images of the reconstruction process is shown in Figure 13. The results of each metric after reconstruction are listed in Table S2 (see Supplementary Materials).

After reconstructing the binarized images, the EAM effectively generated the area of semi-buried nodules, but overfitting remained; the CIM effectively improved the mean and median of the AR and the IoU values (Table S2), and the overall status of their values was the same as the results of Tables 3 and S1. In the binarized images, the EAM effectively reduced the maximum loss of nodule area (Figure 13a): the greater the area of nodule buried by sediment, the better the method works. The CIM retained better reconstruction in the EB and PB types and was more effective in the total sample (Figure 13b).

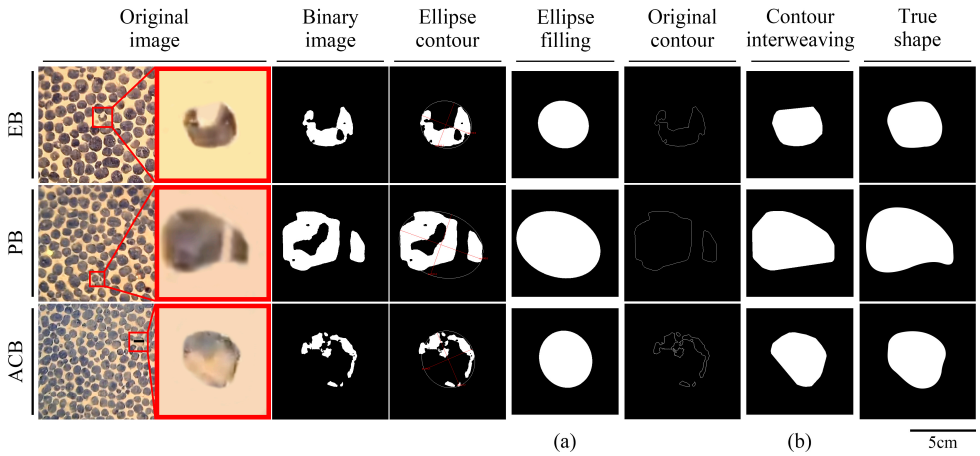


Figure 13. Comparison of different types of semi-buried nodules in binary images: (**a**) image generated by the EAM; (**b**) image generated by the CIM.

5.2. Fusion Experiment

From the Section 4, the CIM and EAM had their own advantages for reconstruction: EAM performed well in the ACB type, while CIM was more prominent in the EB and PB types. To further improve the accuracy of reconstruction, we used the CIM to reconstruct semi-buried nodules of EB and PB types, and the EAM for the ACB type (in binary images). After the two methods were integrated (hereafter referred to as EA-CIM), the performance of each of its indicators was superior to that of EAM and CIM (see Tables S2 and S3 in Supplementary Materials). The EA-CIM allows the maximum and minimum values of each metric to retain the optimal values of the two reconstruction methods, and greatly narrows the distribution ranges of the data to 2.5–97.5%. This suggests that EA-CIM results in a more centralized data set that is closer to the desired values for each metric (Figure 14). Therefore, using different methods for different types of semi-buried nodules allows for further optimization of the reconstruction results.

A seabed global-scale image containing various semi-buried nodule types was reconstructed using the EA-CIM. Compared with the recognition images obtained solely by U-Net training, loss of the semi-buried nodule area was significantly reduced after reconstruction, although some nodules exhibited slight overestimation (Figure 15). It should be noted that we did not extract and reconstruct the semi-buried nodules without the true area as references (see Section 2.3 for the definition).

The areas of different types of nodules were calculated. For EB-type nodules, the recognition rate by U-Net was 71.9%, which increased to 91.35% after reconstruction. For PB type nodules, the rate improved from 58.88% to 92.53%. For ACB-type nodules, the rate rose from 45.7% to 66.28%. Taking the true area as 100%, the EA-CIM enabled a 23.96% increase in the loss area of semi-buried nodules compared with U-Net segmentation. A comparison between U-Net recognition and reconstruction results is summarized in Table 5. In contrast to neural networks that primarily aim to mitigate the impacts of nodule size, color, shape, and imaging illumination on segmentation (such as Mask R-CNN and Pix2PixHD), our approach effectively addresses the inaccuracies in assessment caused by sediment blocking of mineral surfaces in optical images. Our method ensures that the reconstructed nodules exhibit physically plausible continuous surfaces and volumes based on morphological modeling and geometric constraints by targeting the geometric implausibilities frequently encountered in conventional seafloor nodule identification.

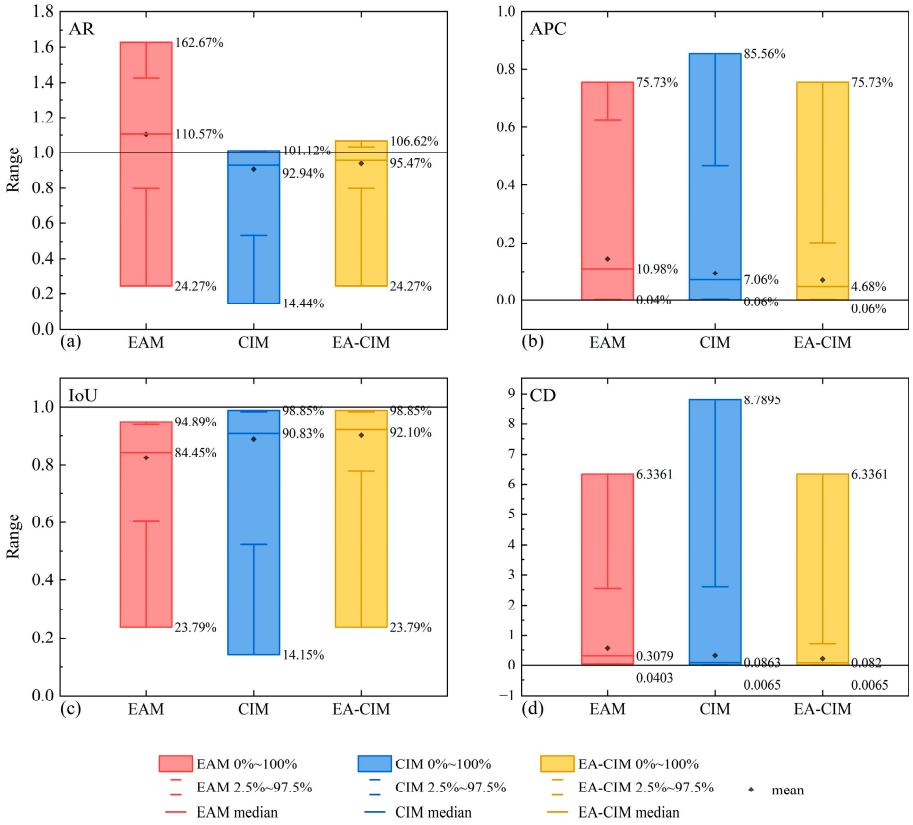


Figure 14. Comparison of the EA-CIM with the two reconstruction methods (binary images): (**a**) distribution of the EAM, CIM, and EA-CIM using the AR metric; (**b**) APC metric; (**c**) IoU metric; (**d**) CD metric.

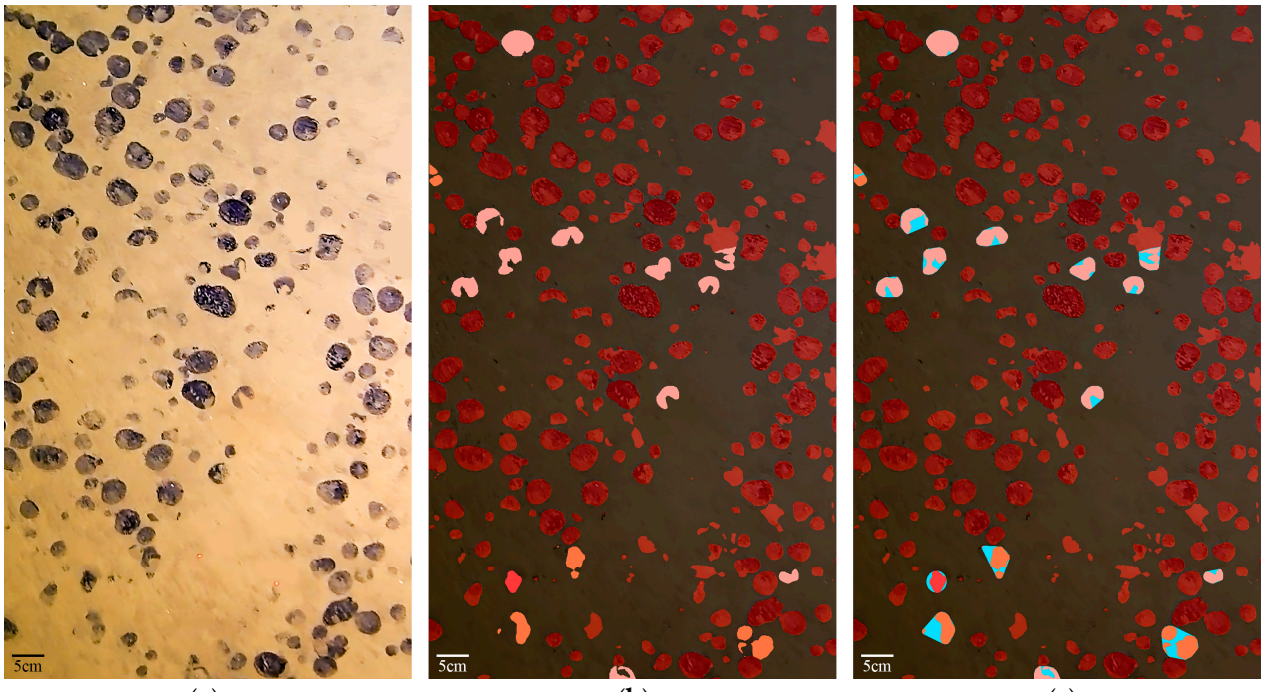


Figure 15. Reconstruction of the EA-CIM in a full image: (**a**) original image after preprocessing; (**b**) large-scale image of PMNs segmented by U-Net; (**c**) overlay of reconstructed shapes of semi-buried nodules with the U-Net recognition result. Cyan, pink, orange, and red represent the restored area by the reconstruction method, the EB type, the PB type, and the ACB type, respectively.

Table 5. Comparison of semi-buried nodule areas identified by U-Net and reconstructed in pixels.

Semi-Buried Type	U-Net Identified Area	Reconstructed Area	TRUE AREA
EB	20,180	25,639	28,067
PB	8272	13,000	14,049
ACB	1297	1881	2838
Total area	29,749	40,520	44,954
AR	66.18%	90.14%	100%

The final reconstruction accuracy exhibited a degree of sensitivity to the pre-defined fusion rules. This was primarily observed in boundary cases where the actual shape of an EB or PB type closely resembled a standard circle or ellipse. In such scenarios, the EAM may yield superior results compared with the CIM, which potentially leads to a measurable improvement in precision. Following the fusion of the methods, some ACB types used with EAM were worse than CIM in some metrics, and EAM improved the results of some EB and PB types (the shape of such nodules was close to the standard circle or ellipse); therefore, defining the scope of the fusion needs to be considered. Possible future directions include automatically determining the reconstruction technique through shape regularity metrics (such as the roundness index) or deep learning networks to further enhance adaptability. The optimal criteria for automatically selecting between EAM and CIM for borderline cases remains an open question for future work.

5.3. Computational Efficiency and Challenges in Method Application

When evaluating algorithm performance, computational efficiency and practical applicability in real-world deployment are equally critical alongside shape-matching accuracy. In terms of computational efficiency, the EAM demonstrated a clear advantage. Its elliptical reconstruction process based on matrix operations exhibits low computational complexity, with approximately 0.011 s required to process a single nodule contour. This makes it suitable for high-volume processing in real-time. In contrast, the CIM involved complex steps such as contour point sampling, matching, and interpolation, which resulted in an average processing time of approximately 0.154 s—15 times longer than the EAM. Testing was conducted on an Intel® Core™ i7-14,700K processor without GPU acceleration. Based on this consequence, and considering the performance ratio between autonomous underwater vehicle (AUV) embedded processors (such as ARM Cortex-A78AE) and the test platform, we calculated the theoretical processing rate of the framework on the target hardware. The estimation indicates that the CIM can handle approximately 1.45 nodules per second, while the EAM can reach 20.4 nodules per second, which provides a quantitative reference for system design. It should be noted that the conversion is based on a single-thread performance ratio, which does not represent the actual runtime of the algorithms on the target platform.

Given the complementary strengths of the EAM and CIM in accuracy and speed, we recommend adopting a layered processing framework to meet the deployment requirements of AUVs. Considering that such platforms typically feature moderately performing embedded processors (such as the ARM Cortex-A series or NVIDIA Jetson series), the current pure CPU implementations of both algorithms already possess basic operational capability [41].

In practical applications, the performance of the CIM was significantly influenced by contour sampling strategies and interpolation parameters. For complex conglomerate nodules featuring deep narrow fissures or branching structures, insufficient or unevenly distributed sampling points may result in incomplete local structure reconstruction, which compromises reconstruction accuracy. In fusion experiments, a single global image takes approximately 2.3 s to process, which meets near-real-time requirements. However, data

processing delays may occur in regions with dense nodule distribution. To meet the requirements of real-time detection and online decision-making for AUVs, we propose adopting an optimization processing strategy based on task layering in actual deployment by performing spatial downsampling on the original acoustic or optical images, and only utilizing CIM for the selected target. Future implementation on embedded hardware will focus on leveraging lightweight parallelization and fixed-point arithmetic to further reduce latency.

6. Conclusions

By combining elliptic approximation and contour interweaving techniques within an adaptive morphology-driven framework, this research presents a robust and practical solution to reconstruct semi-buried PMNs from optical images, and it demonstrates a clear advancement over prior single-method approaches. This dynamic trade-off mechanism significantly enhances the method's practicality and robustness, and it outperforms deep learning models such as U-Net (which only focus on the exposed parts of nodules) in quantitative evaluations. The proposed approach effectively achieves efficient reconstruction of semi-buried nodules and improves the accuracy of resource assessments based on seafloor optical data. It strikes a favorable balance between accuracy, robustness, and computational efficiency, which makes it particularly suitable for online identification and preliminary assessment on computationally constrained platforms such as AUVs. Our key conclusions are as follows:

1. The CIM performs better than the EAM in area and shape dimensions for the reconstruction of semi-buried nodules of the EB and PB types, whereas the EAM is more suitable for the ACB type. However, the EAM carries the risk of overfitting, while the CIM has limited effectiveness in optimizing the metrics for the ACB type.

2. The consistent reconstruction results of the CIM and EAM across different nodule representations (U-Net segmentation and binary image) demonstrate the effectiveness and generalizability of both methods for the three semi-buried nodule types.

3. Integrating the EAM and CIM can significantly enhance PMN resource evaluation accuracy using optical imagery. The EA-CIM can increase the recognized area of the buried nodules from 66.18% to 90.14% compared with the U-Net (with the reference total area set to 100%) and maintain the geometrical stability of the reconstructed nodules. This substantial improvement highlights the considerable potential of the EA-CIM for practical engineering applications.

Future work will focus on optimizing the algorithmic structure of the CIM and exploring adaptive reconstruction strategies based on neural networks to further balance accuracy and efficiency. Concurrently, research will advance from the current two-dimensional projection reconstruction to three-dimensional volume reconstruction. By integrating multi-view images with photometric stereo vision techniques, we aim to construct three-dimensional morphological models of nodules to provide more direct and reliable foundations for resource assessment and mining applications.

Supplementary Materials: The following supporting information can be downloaded at: https://www.mdpi.com/article/10.3390/jmse14030257/s1, Table S1: U-Net versus two reconstruction methods on each metric (boundaries region); Table S2: Binary shapes (BS) versus two reconstruction methods on each metric; Table S3: EA-CIM on each metric (binary images).

Author Contributions: Conceptualization: X.M.; data curation: K.Y., M.W.; funding acquisition: M.W., J.S. and Z.W.; methodology: X.M.; project administration: Q.Y., Z.W.; software: X.M.; supervision: Q.Y., Z.W.; validation: K.Y., M.W. and J.S.; writing—original draft: X.M.; writing—review & editing: K.Y., M.W., Q.Y. and J.S. All authors have read and agreed to the published version of the manuscript.

Funding: This research was funded by National Key Research and Development Program of China, grant numbers 2022YFC2806600 and 2022YFC2806605; National Natural Science Foundation of China, grant number 42306210; Oceanic Interdisciplinary Program of Shanghai Jiao Tong University, grant number SL2023ZD203; and Scientific Research Fund of the Second Institute of Oceanography, Ministry of Natural Resources, China, grant numbers SZ2405 and JG2304.

Data Availability Statement: The data presented in this study are available on request from the corresponding author.

Acknowledgments: We are grateful to all team members of the DY69 cruise for collecting the data, and we also thank the editors and reviewers for their careful review, constructive suggestion and reminding, which helped improve the quality of the paper.

Conflicts of Interest: The authors declare no conflicts of interest.

Abbreviations

The following abbreviations are used in this manuscript:

ACB	almost-completely-buried
APC	absolute percentage change
AR	area ratio
AUV	autonomous underwater vehicle
CD	Chamfer distance
CIM	contour interweaving method
EAM	elliptic approximation method
EB	edge-buried
IB	interior-buried
IoU	intersection-over-union
PB	partition-buried
PMN	polymetallic nodule
TSC	thin-sediment-covering

References

1. Halbach, P.; Fellerer, R. The metallic minerals of the Pacific Seafloor. *GeoJournal* **1980**, *4*, 407–421. [CrossRef]
2. Hein, J.R.; Koschinsky, A.; Kuhn, T. Deep-ocean polymetallic nodules as a resource for critical materials. *Nat. Rev. Earth Environ.* **2020**, *1*, 158–169. [CrossRef]
3. Kuhn, T.; Wegorzewski, A.; Rühlemann, C.; Vink, A. Composition, formation, and occurrence of polymetallic nodules. In *Deep-Sea Mining: Resource Potential, Technical and Environmental Considerations*; Springer: Berlin/Heidelberg, Germany, 2017; pp. 23–63.
4. Hein, J.R.; Mizell, K. Deep-ocean polymetallic nodules and cobalt-rich ferromanganese crusts in the global ocean: New sources for critical metals. In *The United Nations Convention on the Law of the Sea, Part XI Regime and the International Seabed Authority: A Twenty-Five Year Journey*; Brill: Leiden, The Netherlands, 2022; pp. 177–197.
5. Mizell, K.; Hein, J.R.; Au, M.; Gartman, A. Estimates of metals contained in abyssal manganese nodules and ferromanganese crusts in the global ocean based on regional variations and genetic types of nodules. In *Perspectives on Deep-Sea Mining: Sustainability, Technology, Environmental Policy and Management*; Springer: Berlin/Heidelberg, Germany, 2022; pp. 53–80.
6. Miller, K.A.; Thompson, K.F.; Johnston, P.; Santillo, D. An overview of seabed mining including the current state of development, environmental impacts, and knowledge gaps. *Front. Mar. Sci.* **2018**, *4*, 312755. [CrossRef]
7. Meyer, K. Surface sediment and manganese nodule facies encountered on R/V Valdivia cruises 1972/73. *Meerestechnik* **1973**, *4*, 196–199.
8. Meylan, R. *Field Description and Classification of Manganese Nodules*; Technical Report; National Science Foundation (U.S.): Alexandria, VA, USA, 1974.
9. Usui, A. Comparison of Manganese Nodules from the Northest Equatorial Pacific (Cruise SO 25) with Nodules from the Central Pacific Basin. *Geol. Jb.* **1987**, *87*, 287–313.
10. Vineesh, T.; Nagender Nath, B.; Banerjee, R.; Jaisankar, S.; Lekshmi, V. Manganese nodule morphology as indicators for oceanic processes in the Central Indian Basin. *Int. Geol. Rev.* **2009**, *51*, 27–44. [CrossRef]

11. Yoo, C.M.; Joo, J.; Lee, S.H.; Ko, Y.; Chi, S.-B.; Kim, H.J.; Seo, I.; Hyeong, K. Resource assessment of polymetallic nodules using acoustic backscatter intensity data from the Korean exploration area, northeastern equatorial pacific. *Ocean Sci. J.* **2018**, *53*, 381–394. [CrossRef]
12. Alevizos, E.; Schoening, T.; Koeser, K.; Snellen, M.; Greinert, J. Quantification of the fine-scale distribution of Mn-nodules: Insights from AUV multi-beam and optical imagery data fusion. *Biogeosci. Discuss.* 2018, *in review*.
13. Prabhakaran, K.; Ramesh, R.; Rajesh, S.; Gopakumar, K.; Ramadass, G.; Atman, M. Underwater Image Processing to Detect Polymetallic Nodule Using Template Matching. In Proceedings of the Global Oceans 2020: Singapore—US Gulf Coast, Biloxi, MS, USA, 5–30 October 2020; pp. 1–6.
14. Schoening, T.; Jones, D.O.; Greinert, J. Compact-morphology-based poly-metallic nodule delineation. *Sci. Rep.* **2017**, *7*, 13338. [CrossRef]
15. Dong, L.; Wang, H.; Song, W.; Xia, J.; Liu, T. Deep sea nodule mineral image segmentation algorithm based on Mask R-CNN. In Proceedings of the ACM Turing Award Celebration Conference-China, Hefei, China, 30 July–1 August 2021; pp. 278–284.
16. Song, W.; Wang, H.; Zhang, X.; Xia, J.; Liu, T.; Shi, Y. Deep-sea Nodule Mineral Image Segmentation Algorithm Based on Pix2PixHD. *Comput. Mater. Contin.* **2022**, *73*, 1449. [CrossRef]
17. Shao, M.; Song, W.; Zhao, X. Polymetallic nodule resource assessment of seabed photography based on denoising diffusion probabilistic models. *J. Mar. Sci. Eng.* **2023**, *11*, 1494. [CrossRef]
18. Tomczak, A.; Kogut, T.; Kabała, K.; Abramowski, T.; Ciążela, J.; Giza, A. Automated estimation of offshore polymetallic nodule abundance based on seafloor imagery using deep learning. *Sci. Total Environ.* **2024**, *956*, 177225. [CrossRef]
19. Verlaan, P.A.; Cronan, D.S. Origin and variability of resource-grade marine ferromanganese nodules and crusts in the Pacific Ocean: A review of biogeochemical and physical controls. *Geochemistry* **2022**, *82*, 125741. [CrossRef]
20. Tsune, A. Quantitative expression of the burial phenomenon of deep seafloor manganese nodules. *Minerals* **2021**, *11*, 227. [CrossRef]
21. Alevizos, E.; Huvenne, V.A.; Schoening, T.; Simon-Lledó, E.; Robert, K.; Jones, D.O. Linkages between sediment thickness, geomorphology and Mn nodule occurrence: New evidence from AUV geophysical mapping in the Clarion-Clipperton Zone. *Deep Sea Res. Part I Oceanogr. Res. Pap.* **2022**, *179*, 103645. [CrossRef]
22. Wasilewska-Błaszczyk, M.; Mucha, J. Possibilities and limitations of the use of seafloor photographs for estimating polymetallic nodule resources—Case study from IOM Area, Pacific Ocean. *Minerals* **2020**, *10*, 1123. [CrossRef]
23. Deng, J.; Wang, X.; Wang, H.; Cao, H.; Xia, J. Quantitative Description of Size and Mass Distribution of Polymetallic Nodules in Northwest Pacific Ocean Basin. *Minerals* **2024**, *14*, 1230. [CrossRef]
24. Li, N.; Zou, T.; Cheng, Y.; Li, H. A method for evaluating the abundance of deep-sea polymetallic nodules based on image processing. *Ocean Eng.* **2025**, *43*, 76–88. [CrossRef]
25. Sharma, R. Effect of Sediment-Water Interface 'Boundary Layer' on Exposure of Nodules and Their Abundance: A Study from Seabed Photos. *J. Geol. Soc. India* **1989**, *34*, 310–317. [CrossRef]
26. Song, W.; Dong, L.; Zhao, X.; Xia, J.; Liu, T.; Shi, Y. Review of Nodule Mineral Image Segmentation Algorithms for Deep-Sea Mineral Resource Assessment. *Comput. Mater. Contin.* **2022**, *73*, 1649. [CrossRef]
27. Tsune, A. Effects of size distribution of deep-sea polymetallic nodules on the estimation of abundance obtained from seafloor photographs using conventional formulae. In Proceedings of the ISOPE Ocean Mining and Gas Hydrates Symposium, Kona, HI, USA, 21–26 June 2015; p. ISOPE-M-15-241.
28. Song, W.; Zheng, N.; Liu, X.; Qiu, L.; Zheng, R. An improved u-net convolutional networks for seabed mineral image segmentation. *IEEE Access* **2019**, *7*, 82744–82752. [CrossRef]
29. Ronneberger, O.; Fischer, P.; Brox, T. U-net: Convolutional networks for biomedical image segmentation. In Proceedings of the International Conference on Medical Image Computing and Computer-Assisted Intervention, Munich, Germany, 5–9 October 2015; pp. 234–241.
30. Tejada, P.J.; Qi, X.; Jiang, M. Computational Geometry of Contour Extraction. In Proceedings of the CCCG, Montreal, QC, Canada, 10–12 August 2009; pp. 25–28.
31. Serra, J.; Soille, P. *Mathematical Morphology and Its Applications to Image Processing*; Springer Science & Business Media: Berlin/Heidelberg, Germany, 2012; Volume 2.
32. Soille, P. *Morphological Image Analysis: Principles and Applications*; Springer: Berlin/Heidelberg, Germany, 1999; Volume 2.
33. Pratt, W.K. *Digital Image Processing: PIKS Scientific Inside*; Wiley Online Library: Hoboken, NJ, USA, 2007; Volume 4.
34. Benites, M.; Millo, C.; Hein, J.; Nath, B.N.; Murton, B.; Galante, D.; Jovane, L. Integrated geochemical and morphological data provide insights into the genesis of ferromanganese nodules. *Minerals* **2018**, *8*, 488. [CrossRef]
35. Liu, B.; Wang, X.; Zhang, X.; Liu, J.; Rong, L.; Ma, Y. Research status of deep-sea polymetallic nodule collection technology. *J. Mar. Sci. Eng.* **2024**, *12*, 744. [CrossRef]
36. Bresenham, J.E. Algorithm for computer control of a digital plotter. In *Seminal Graphics: Pioneering Efforts That Shaped the Field*; Association for Computing Machinery (ACM): New York, NY, USA, 1998; pp. 1–6.

37. Girshick, R.; Donahue, J.; Darrell, T.; Malik, J. Rich feature hierarchies for accurate object detection and semantic segmentation. In Proceedings of the IEEE Conference on Computer Vision and Pattern Recognition, Columbus, OH, USA, 23–28 June 2014; pp. 580–587.
38. Borgefors, G. Distance transformations in digital images. *Comput. Vis. Graph. Image Process.* **1986**, *34*, 344–371. [CrossRef]
39. Ma, T.; Yang, X.; Latecki, L.J. Boosting chamfer matching by learning chamfer distance normalization. In Proceedings of the European Conference on Computer Vision, Crete, Greece, 5–11 September 2010; pp. 450–463.
40. Myronenko, A.; Song, X. Point set registration: Coherent point drift. *IEEE Trans. Pattern Anal. Mach. Intell.* **2010**, *32*, 2262–2275. [CrossRef] [PubMed]
41. Zacchini, L.; Ridolfi, A.; Topini, A.; Secciani, N.; Bucci, A.; Topini, E.; Allotta, B. Deep learning for on-board AUV automatic target recognition for optical and acoustic imagery. *IFAC-PapersOnLine* **2020**, *53*, 14589–14594. [CrossRef]

Disclaimer/Publisher's Note: The statements, opinions and data contained in all publications are solely those of the individual author(s) and contributor(s) and not of MDPI and/or the editor(s). MDPI and/or the editor(s) disclaim responsibility for any injury to people or property resulting from any ideas, methods, instructions or products referred to in the content.